JOURNAL OF GUIDANCE, CONTROL, AND DYNAMICS
Vol. 27, No. 2, March–April 2004

Dynamics and Stability of an Autorotating Rotor/Wing Unmanned Aircraft

C. A. Lopez* and V. L. Wells†
Arizona State University, Tempe, Arizona 85287-6106

The development of and results from a dynamic analysis of a hybrid autorotating rotor/wing aircraft are presented. The aircraft is intended for use as an unmanned reconnaissance vehicle to be air launched from the pylon of a base aircraft. The rotor/wing aircraft may be operated as a conventional, fixed-wing airplane or as an autogyro for low-speed surveillance and landing. Analysis presented includes dynamic stability and control features of the autogyro configuration. Generally, the autogyro exhibits dynamic modes characteristic of a conventional aircraft with the exception of an additional, slowly convergent mode associated with the rotor angular velocity degree of freedom. The rotor angular velocity also plays an important role in the unstable autogyro phugoid mode. Control effectiveness in the autorotating configuration is generally good, though it is recommended that the rotor longitudinal cyclic control be assisted by the elevons to enhance control power in pitch.

Nomenclature

A	=	state-space linearized system matrix
A_1, B_1	=	lateral and longitudinal cyclic control, deg
A_{blades}, A_{disk}	=	area of rotor/wing blades and rotor/wing disk, m^2
a_{1s}, b_{1s}	=	longitudinal and lateral flapping angles
$a_{Lw\_\alpha\_3D}$	=	lift curve slope of rotor/wing airfoil section, 1/rad
B	=	state-space linearized controllability matrix
C_H	=	rotor/wing horizontal-force (H-force) coefficient
C_Q	=	rotor/wing torque coefficient
C_T	=	rotor/wing thrust coefficient
c_d	=	parasite drag coefficient of rotor/wing airfoil section
c_W	=	average cord of rotor/wing airfoil section, m
D_F, D_{HS}, D_{VS}, D_W	=	drag due to fuselage, horizontal stabilizers, vertical stabilizers, and wing, N
Fs_F, Fs_{VS}	=	side lift due to fuselage and vertical stabilizers, N
F_x, F_y, F_z	=	aerodynamic forces acting on the aircraft body axes system, N
g	=	Earth specific gravitational constant, m/s^2
H_M	=	horizontal force generated by the rotor/wing, N
H'_x, H'_y, H'_z	=	additional rotor angular momentum components
H'_{x_prop}, H'_{z_rotor}	=	angular momentum components due to propeller and rotor/wing, kg · m^2/s
I_b	=	mass moment of inertia of rotor/wing blade
I_x, I_y, I_z	=	aircraft mass moments of inertia about the body axes, kg · m^2
I_{xz}	=	aircraft product of inertia, kg · m^2
i_M	=	incidence angle of rotor/wing and rotor shaft, rad
J	=	polar moment of inertia of rotor/wing, kg m^2
L_F, L_{HS}, L_W	=	lift due to fuselage, horizontal stabilizers, and wing, N
$l_{x\_\text{ac}\_(\,)}$, $l_{y\_\text{ac}\_(\,)}$, $l_{z\_\text{ac}\_(\,)}$	=	components of location of surface aerodynamic center relative to aircraft center of gravity, m
$l_{x\_M\text{Rac}}$, $l_{y\_M\text{Rac}}$, $l_{z\_M\text{Rac}}$	=	components of location of rotor/wing center relative to aircraft center of gravity, m
M_w, M_Ω	=	aircraft pitching moment vs w and Ω derivatives
M_x, M_y, M_z	=	aerodynamic moments acting about the aircraft body axes system, N · m
$M_{x\_\text{HS}\_p}$, $M_{x\_W\_p}$	=	aerodynamic rolling moment due to roll-rate generated by the horizontal stabilizer and wing, N · m
$M_{y\_F\_mrp}$, $M_{y\_\text{HS}\_ac}$, $M_{y\_W\_ac}$	=	aerodynamic pitching moment generated by the fuselage, horizontal stabilizers, and wing, N · m
$M_{z\_F\_mrp}$, $M_{z\_\text{VS}\_ac}$	=	aerodynamic yawing moment generated by the fuselage and vertical stabilizers, N · m
m	=	specific mass, kg
N_{half}	=	dynamic mode cycles to half or double
p, q, r	=	angular velocity components about body axes, rad/s
Q_M, Q_{prop}	=	torque generated by rotor/wing and propeller, N · m
Q_u	=	rotor/wing torque versus u derivative
R_{blade}	=	radius of rotor/wing blade, m
T	=	dynamic mode period, s
T_M	=	thrust generated by the rotor/wing, N
T_{prop}	=	thrust generated by turboprop engine, N
t_{half}	=	dynamic mode time to half or double, s
$\boldsymbol{u}$	=	state-space input vector
u, v, w	=	translational velocity components along body axes, m/s

Received 7 March 2003; revision received 5 August 2003; accepted for publication 5 August 2003.

*Graduate Research Assistant, Department of Mechanical and Aerospace Engineering. Member AIAA.
†Associate Professor, Department of Mechanical and Aerospace Engineering, Box 876106. Associate Member AIAA.

V_∞, V_{∞_nd}	=	aircraft airspeed, actual and nondimensional
v_i, v_{i_hover}, v_{i_nd}	=	rotor/wing induced velocity, actual, at hover, and nondimensional
$\boldsymbol{x}$	=	state-space state vector
x_b, y_b, z_b	=	components of body axis system
x_e, y_e, z_e	=	components of inertial axis system
$\boldsymbol{y}$	=	state-space output vector
α, α_s, α_{TPP}, α_t	=	angle of attack of fuselage, rotor shaft, tip-path plane, tail, rad
β	=	sideslip angle, rad; rotor/wing blade flapping angle, rad
γ	=	aircraft flightpath angle, deg
γ_b	=	Lock number of rotor/wing blade
δ_{e_L}, δ_{e_R}, δ_r	=	control inputs for left and right elevon deflection, and rudder deflection, deg
θ_o	=	collective pitch of rotor/wing blades, deg
λ'	=	inflow ratio of rotor/wing tip-path plane
μ	=	rotor/wing tip-speed ratio
ρ	=	air density at sea level
σ	=	solidity ratio of the rotor/wing
ϕ, θ	=	roll and pitch attitude, rad
ψ	=	yaw attitude, rad; rotor/wing azimuth angle, rad
Ω	=	rotor/wing angular velocity, rad/s

I. Introduction

THE air-launched, self-recovering autonomous vehicle (ALSR AV)[1] was initially designed to address the needs of the U.S. Army's Airborne Manned–Unmanned System Technology program, which envisions unmanned autonomous vehicles (UAVs) operating in cooperation with attack helicopters. The ALSR AV employs the rotor/wing concept that enables it to fly as a conventional fixed-wing aircraft or as an autogyro (AG). The unmanned aircraft is carried on a wing-mounted pylon of the helicopter; in this case the AH-64 Apache is used as an example. This reduces the fuel requirement of the UAV because it is transported to the area of operation and maximizes the flexibility of its launch and subsequent operation. The pilots of the helicopter can launch the ALSR AV at will. Separate launching facilities or locations are not required, although remote launch and recovery capability is possible with the current concept. Other air-launched UAVs are typically recovered with parachutes, making precision recovery and rapid turnaround difficult. The aircraft rotor is aerodynamically driven, which simplifies the design of the rotor/wing hub and the propulsion system and eliminates the need for an antitorque device. Recovering the aircraft as an AG allows operations in a small area. The ALSR AV concept provides the flexibility of an air-launched vehicle, the endurance properties of a fixed-wing vehicle, and the restricted recovery area of a helicopter.[2]

Figure 1 (Ref. 2) shows the three-view layout of the ALSR AV. The fuselage of the aircraft is designed to include and support the propulsion system, rotor/wing shaft and mechanisms, fuel system (volume for 170 lb of fuel), retractable landing gear, avionics systems, sensors, and data transmitters. Lateral and longitudinal control (roll and pitch) is provided by elevons embedded in the horizontal stabilizer. Yaw stability is provided by three vertical tails, including two small vertical stabilizers located at each end of the horizontal stabilizer and a large inverted vertical stabilizer located in the center of the fuselage tail. The center-inverted vertical stabilizer has a rudder control surface to aid lateral control (yaw and roll). The aircraft utilizes either a turboprop or a turbofan engine depending on the requirements of the mission. The layout shown in Fig. 1 is for the turboprop configuration.

The rotor/wing is located near the center of the fuselage, slightly aft of the center of gravity. It consists of two blades secured to a

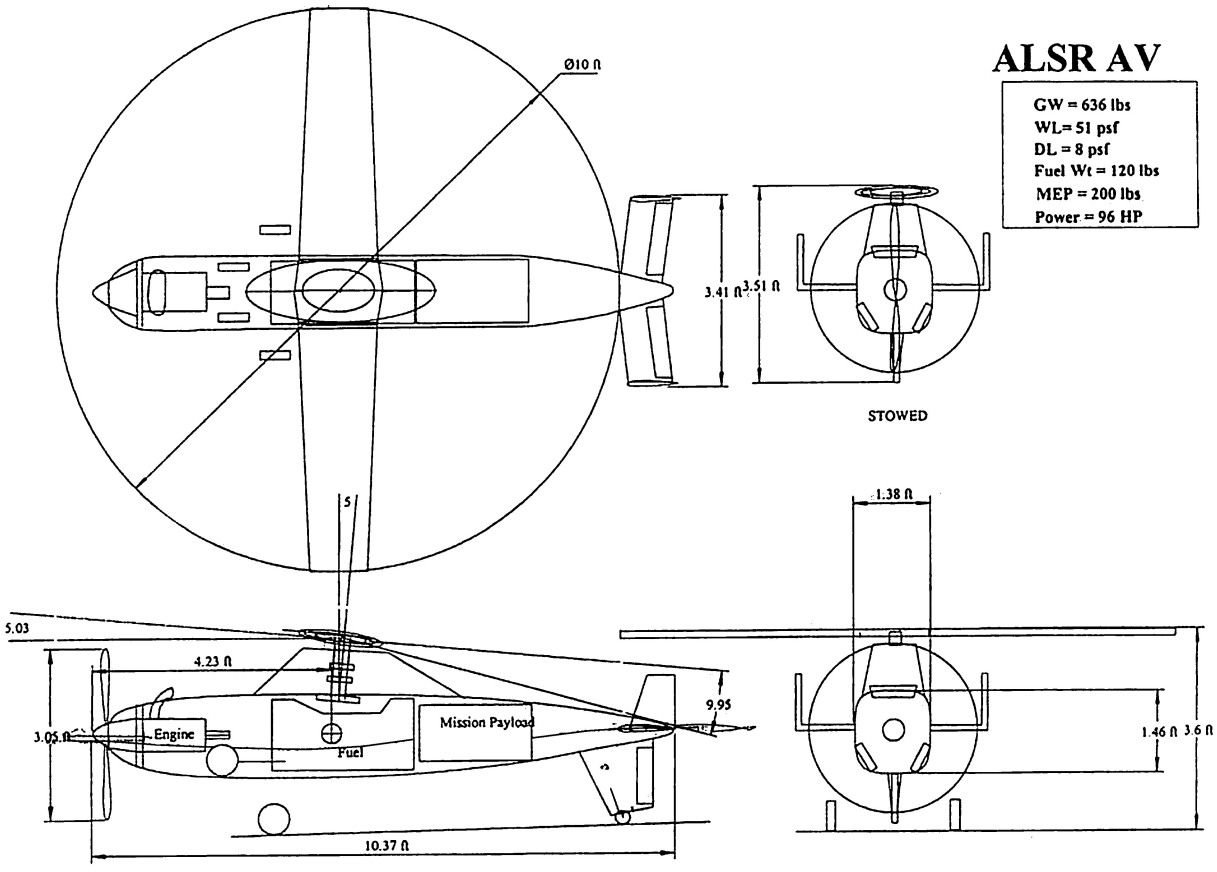

Fig. 1 ALSR AV configuration (layout of vehicle).

rotor shaft that is tilted 5 deg aft. The airfoil cross sections are elliptical (fore–aft symmetrical) with blunt trailing edges. The fore–aft symmetrical airfoil permits the rotor wing to function as a fixed wing when locked perpendicular to the fuselage, or as a rotor when released. The structure of the rotor blades is rigid so that it does not require centrifugal stiffening as in the case of a typical helicopter rotor blade. The two rotor blades are secured by a central hub that incorporates a mechanism with a torsional spring that locks the rotor/wing along the fuselage axis in the stowed position, reconfigures the wing orthogonal to the fuselage axis for conventional flight, and finally releases the rotor/wing to spin as an AG with cyclic and collective pitch control for landing. When operating as an AG, the rotor eliminates rolling moments by teetering. In conventional fixed-wing mode, the rotor hub mechanism suppresses the teetering and locks the collective pitch control.[1,2] The Boeing Company canard rotor/wing (CRW) concept, designated X-50A Dragonfly,[‡] uses a similar rotor/wing device. However, unlike the freely windmilling rotor of the ALSR AV, the Dragonfly rotor uses tip reaction drive provided by a single turbofan engine to power the rotating rotor/wing.

A more complete description of the UAV's proposed flight operation, as well as an initial estimate of its performance characteristics, is given in Ref. 2.

The AG has not enjoyed a great deal of popularity in recent years. Perhaps because of this, there exists very little analysis of its dynamic behavior. However, Houston[3] has identified some basic characteristics of AG stability and dynamic modes. Using a state-space analysis that found stability derivatives through experimental system identification, he showed that the example gyroplane (a VPM M16 kit AG) exhibits classical and stable longitudinal dynamic modes. He introduced an additional degree of freedom, associated with the rotor angular velocity, which he terms the "rotor-speed" mode and which is coupled with the classical aircraft degrees of freedom. Later analysis uses a general rotorcraft analytical model for rotor-induced velocity.[4] Results from this investigation indicate some discrepancies between the simulation and the experimental behavior of the vehicle, particularly in the lateral (Dutch-roll) response.

This paper takes a slightly different approach in that rotor-induced velocity is assumed to be distributed according to the simple equation, $v_1 = v_{1_{av}}(1 + r/R\cos\psi)$ where, here, ψ represents the rotor azimuth and $v_{1_{av}}$ is determined according to a momentum theory valid for all tip-path-plane angles. Note that this distribution provides only a fore–aft variation in induced velocity, unlike the model used in Ref. 4, which has an additional term in $\sin\psi$ accounting for lateral variation in v_1. The current model allows the rotor forces and moments to be integrated over all blades into closed-form equations, thereby simplifying solution of the aircraft dynamics. Comparison of the current results with those of Houston[3] indicates that the basic dynamic characteristics of the aircraft are intact regardless of which inflow condition is used. The rotor/wing is treated as a single, teetering, rotating lifting surface that is allowed to flap according to the instantaneous aerodynamic and inertial moments about the teetering hinge. In the sense that the current equations consider only the steady-state or particular solution, the flapping inertia (homogeneous solution) is not modeled.

The paper presents the development of the ALSR AV nonlinear equations of motion and the dynamic modes for autorotative flight and assesses the stability, open-loop control response and control effectiveness of the aircraft in AG configuration. First, the dynamics and aerodynamics of the rotor/wing operating as a teetering rotor are investigated. An approach consisting of using a one-degree-of-freedom (1-DOF) equation of motion along with closed-form equations is used to model the rotor/wing dynamics and aerodynamics. The rotor/wing dynamic equations are incorporated into the conventional aircraft's 6-DOF nonlinear equations of motion to model the AG ALSR AV dynamics. The models are verified by observing their predicted responses to given control inputs. Three equilibrium points for the ALSR AV in AG configuration are determined using a trim code with a multivariable minimization algorithm at its core. The nonlinear systems are linearized, thus obtaining state-space models at each equilibrium point. The validity of the linear systems is assessed by comparing the linear and the nonlinear responses. Stability analysis to small disturbances is performed at each equilibrium point, and the dynamic modes of the aircraft in autorotative flight are investigated. Six dynamic modes for the AG configuration are identified and analyzed. It is also investigated how the poles of the dynamic modes move as the airspeed of the aircraft increases or decreases (effect of airspeed on AG flight stability). Finally, an open-loop control analysis is performed. The effect of the dynamic modes on the responses of the aircraft to selected control inputs is investigated. Also, the effectiveness of the ALSR AV controls on the attitude of the aircraft in AG flight is explored.

Note that a complete analysis of the ALSR AV in fixed-wing flight has been completed. Because the development is conventional in nature, it is not included. However, some results from the fixed-wing analysis are briefly discussed for purposes of validating the model and for completeness in the assessment of the aircraft control response.

II. Equations of Motion for Autorotative Flight

The equations of motion for the ALSR AV in conventional flight, valid in the aircraft-fixed frame of reference (body axes), are derived, for example, by Etkin and Reid.[5] These equations are quite general and their derivation makes the following assumptions:

1) The airplane is a rigid body, which may have attached to it any number of rigid spinning rotors.

2) The xz plane is a plane of mirror symmetry, so that $I_{yz} = I_{xy} = 0$.

3) The axes of any spinning rotors are fixed in direction relative to the body axes, and the rotors have constant angular speed relative to the body axes.

Operating as a fixed-wing aircraft, the ALSR AV produces aerodynamic forces and moments in a mostly conventional manner with contributions from the fuselage, tails, wing, and propeller. In AG mode, however, an additional DOF corresponding to the rotor angular velocity must be introduced to account for item 3, which does not hold when the rotor speed varies.

In autorotation mode, the rotor/wing is mounted on a rotor shaft that is tilted 5 deg aft to increase the tip-path-plane angle of attack α_{TPP}. The rotor/wing has angular velocity Ω, a function of the rotor tip-path-plane angle α_{TPP}; the rotor control variables A_1, B_1, and θ_o; and the aircraft state u, v, w, p, q, and r. The cyclic, A_1, B_1, and collective, θ_o, control inputs to the rotating rotor/wing are defined in the same way as those for a conventional helicopter rotor.[6] Q_M represents the aerodynamic torque about the rotor shaft. In steady-state AG operation, the net Q_M equals zero because the aerodynamic driving force on the rotor is in equilibrium with the drag generated by the rotor blades. The torque transmitted from the rotor/wing to the fuselage is assumed to be zero at all times, implying a frictionless rotor-shaft bearing. The thrust T_M generated by the rotor is composed of the lift and drag components of the rotor blade perpendicular to the tip-path plane. T_M as a resultant vector acts at a longitudinal angle a_{1s} with respect with to the z axis of the rotor shaft reference frame z_s and at a lateral angle b_{1s} with respect to the same axis. The rotor horizontal force H_M acts in the rotor tip-path plane in the direction of the negative x_b axis and is generated by the components of rotor lift and rotor drag acting in this direction.

When the ALSR AV is operating in AG mode, forces and moments arising from the rotating blades replace conventional wing lift and drag effects in the equations of motion. Rotor/wing forces and moments expressions are derived with the help of Ref. 6 as

[‡]Additional data about The Boeing Company Phantom Works CRW may be found at http://www.boeing.com/phantom/crw.html [cited 28 September 2002].

$$
\begin{aligned}
F_x &= -H_M \cos(a_{1s} + i_M) - T_M \sin(a_{1s} + i_M)\\
F_y &= T_M \sin b_{1s} - H_M \sin\beta\\
F_z &= -T_M \cos(a_{1s} + i_M)\\
M_x &= [T_M \sin b_{1s} - H_M \sin\beta] l_{z\_M\mathrm{Rac}} + Q_M \sin(a_{1s} + i_M)\\
&\quad + [-T_M \cos(a_{1s} + i_M)] l_{y\_M\mathrm{Rac}}\\
M_y &= [-H_M \cos(a_{1s} + i_M) - T_M \cos(a_{1s} + i_M)] l_{z\_M\mathrm{Rac}}\\
&\quad + [-T_M \cos(a_{1s} + i_M)] l_{x\_M\mathrm{Rac}} - Q_M \sin b_{1s}\\
M_z &= -[T_M \sin b_{1s} - H_M \sin\beta] l_{x\_M\mathrm{Rac}} + Q_M \cos(a_{1s} + i_M) \cos b_{1s}
\end{aligned} \tag{1}
$$

The rotor forces and flapping angles all depend on the rotor angular velocity Ω, which is introduced as a new state variable. The equation representing the rotational dynamics of the rotor is approximated as

$$\dot{\Omega} = -Q_M / J$$

To neglect the additional acceleration terms, note that for all cases examined $\Omega \gg p, q, r$. The Coriolis acceleration, $2\Omega\dot{\beta}_f \sin(\beta_f)$, causes a high-frequency superposition on the rotor rotational velocity, but only a very small deviation in the aircraft dynamic response. It is, therefore, not considered in the following analysis.

The rotor torque Q_M is computed from the equations of Prouty,[6] who utilizes several simplifying assumptions to allow for a closed-form solution. Chief among these assumptions is the predefined distribution of rotor-induced velocity (as described earlier). The torque coefficient (of the rotor/wing) over solidity ratio σ is given as

$$
\begin{aligned}
C_Q/\sigma &= c_d/8(1+\mu^2)\\
&\quad - \left\{a\lambda' \Big/ \left[4\left(1 + \tfrac{3}{2}\mu^2\right)\right]\right\}\left\{\theta_o/3(2-\mu^2) + \lambda'[1 + (\mu^2/2)]\right\}
\end{aligned} \tag{2}
$$

The torque acting on the rotor comes from making the preceding expression dimensional:

$$Q_M = (C_Q/\sigma)\rho A_{\mathrm{blades}} (\Omega R_{\mathrm{blade}})^2 R_{\mathrm{blade}}$$

The right-hand side of Eq. (2) has a complicated dependence on the state variables Ω, p, q, u, v, and w through the advance ratio, $\mu = V_\infty / \Omega R_{\mathrm{blade}}$, and particularly the inflow ratio, $\lambda' = \mu\alpha_{\mathrm{TPP}} - v_i / \Omega R_{\mathrm{blade}}$. In Ref. 7, the details of the specific dependence of α_{TPP} and v_i on the state variables are given.

The remaining rotor forces and flapping coefficients are computed in a similar manner. Prouty's analysis yields:

$$
\begin{aligned}
a_{1s} &= \left(\frac{\mu}{1 + \frac{1}{2}\mu^2}\right)\left[\frac{8}{3}\theta_o + 2\left(\mu\alpha_s - \frac{v_i}{\Omega R_{\mathrm{blade}}}\right)\right]\\
&\quad - \left[\frac{1 + (3/2)\mu^2}{1 - (1/2)\mu^2}\right] B_1 + \frac{-16/\gamma_b (q/\Omega) + (p/\Omega)}{1 - (1/2)\mu^2}
\end{aligned} \tag{3}
$$

$$
\begin{aligned}
b_{1s} &= A_1 + \frac{v_i/\Omega R_{\mathrm{blade}}}{1 + (1/2)\mu^2} + \frac{-16/\gamma_b (p/\Omega) - (q/\Omega)}{1 + (1/2)\mu^2}\\
C_T/\sigma &= \frac{a}{4[1 + (3/2)\mu^2]}\left\{\left(\frac{2}{3} - \frac{2}{3}\mu^2 + \frac{3}{2}\mu^4\right)\theta_o + \left(1 - \frac{\mu^2}{2}\right)\lambda'\right\}\\
\frac{C_H}{\sigma} &= \frac{1}{\mu}\left[\frac{c_d}{8}(1 + 3\mu^2) - \lambda'\frac{C_T}{\sigma} - \frac{C_Q}{\sigma}\right]
\end{aligned} \tag{4, 5}
$$

$$
\begin{aligned}
T_M &= (C_T/\sigma)\sigma\rho A_{\mathrm{disk}} (\Omega R_{\mathrm{blade}})^2\\
H_M &= (C_H/\sigma)\sigma\rho A_{\mathrm{disk}} (\Omega R_{\mathrm{blade}})^2
\end{aligned}
$$

III. Model Verification

In the absence of a working vehicle or wind-tunnel data, the ALSR AV AG model is verified by analyzing the response of the aircraft to the rotor/wing control inputs θ_o, A_1, and B_1. The flight conditions described in Table 1 provide the trim points about which the response is computed. The response to increment in collective pitch, $\delta\theta_o = 0.25$ deg, is that a positive collective pitch control input increases the pitch of the rotor/wing blades. The collective pitch control input is applied after 1 s of steady-state level flight at 34, 53, and 75 m/s.

Figure 2 shows rotor speed Ω response at all three trim points. Of interest is the differing initial response (increasing or decreasing Ω) depending on the initial conditions. At low advance ratio, the rotor immediately slows down when the collective angle increases, whereas at higher advance ratio, the rotor initially speeds up. The rotor acceleration depends on the sign of the aerodynamic torque produced as a result of the collective input. At equilibrium, the rotor torque [Eq. (2)] must equal zero, but when the collective increases, the rotor torque is no longer balanced. Both drag torque $[c_d/8(1+\mu^2)]$ and driving torque

$$\frac{a\lambda'}{4[1 + (3/2)\mu^2]}\left[\frac{\theta_o}{3}(2 - \mu^2) + \lambda'\left(1 + \frac{\mu^2}{2}\right)\right]$$

are altered with increasing θ_0, and the sign of the resulting torque depends on which term dominates for the given flight conditions. For an AG, $\lambda' = \mu\alpha_{\mathrm{TPP}} - v_i/\Omega R$ is always positive; in fact, it is clear from Eq. (2) that the torque could never equal zero (trim) unless this is the case. The dimensionless average induced velocity $v_i/\Omega R$ varies approximately as $C_T/2\mu$. Any variations in advance ratio (due to $\delta\theta_o$) are secondary and not explicitly a function of the change in collective; thus, the change in inflow can be written as

$$\Delta\lambda' = \mu\Delta\alpha_{\mathrm{TPP}} - \Delta C_T/2\mu \tag{6}$$

For the three cases tested, the $\Delta\lambda'$ in response to the increasing collective is negative at low advance ratio ($\mu = 0.22$) and is positive at the higher μ values.

Table 1 Trim of autogyro aircraft at 34, 53, and 75 m/s level flight

Parameter	Initial state x_o {34, 53, 75} m/s	Parameter	Control inputs u {34, 53, 75} m/s
u	[34, 53, 75] m/s	δ_r	[0, 0, 0] deg
v	[0, 0, 0] m/s	δ_{e_L}	[0, 0, 0] deg
w	[2.86, 1.32, 1.68] m/s	δ_{e_R}	[0, 0, 0] deg
p	[0, 0, 0] rad/s	T_{prop}	[998.25, 715.43, 793.38] [N]
q	[0, 0, 0] rad/s	θ_o	[6.11, 7.28, 8.85] deg
r	[0, 0, 0] rad/s	A_1	[−3.23, −2.29, −1.78] deg
x_e	[0, 0, 0] [m]	B_1	[−4.48, 2.95, 7.75] deg
y_e	[0, 0, 0] [m]		
z_e	[0, 0, 0] [m]		
ϕ	[0, 0, 0] deg		
θ	[4.80, 1.43, 1.28] deg		
ψ	[0, 0, 0] deg		
Ω	[100, 100, 100] rad/s		

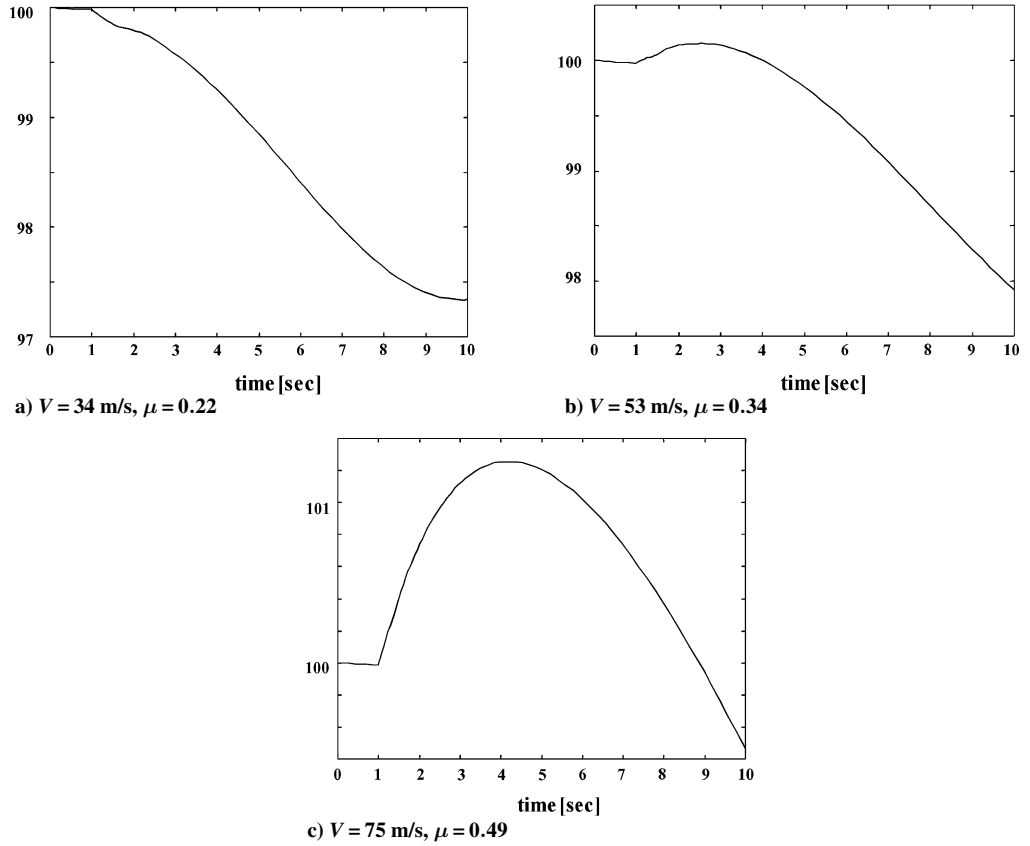

a) $V = 34$ m/s, $\mu = 0.22$ b) $V = 53$ m/s, $\mu = 0.34$

c) $V = 75$ m/s, $\mu = 0.49$

Fig. 2 Rotor speed response to collective angle input, $\delta\theta_0 = 0.25$ deg; vertical axis is rotor angular velocity in radians per second.

To see why this is so, consider that an increase in collective increases the C_T approximately the same amount regardless of trim advance ratio, so that ΔC_T varies only minimally with μ. The same statement can be made about the change in tip-path-plane angle; though $\Delta\alpha_{\text{TPP}}$ is larger for higher μ, it does not vary greatly as a function of advance ratio. It is then clear from Eq. (6) that the influence of the advance ratio is to emphasize the positive term for high μ (linear relationship) and the negative term for low μ (inverse dependence). This is simply a statement that, as advance ratio increases, the rotor inflow becomes more dependent on the vehicle forward speed rather than on the induced velocity, a result that could be deduced based on the known behavior of v_i as the forward velocity increases.

Because c_d virtually always increases with increasing collective, it is apparent that the drag torque will dominate the driving torque for $\mu = 0.22$, for which case the $\Delta\lambda'$ (and, thus, the driving torque) is decreased. However, once the advance ratio is high enough that $\Delta\lambda' > 0$, the sign of the rotor torque will depend on which torque component experiences the higher increase. According to the results presented in Fig. 2, once the advance ratio reaches $\mu = 0.34$, the driving torque is larger than the drag torque, and the rotor speed increases in response to a collective increase.

Note that the simple induced-velocity representation used in this model becomes less accurate as advance ratio increases because of the larger region of reverse flow on the retreating rotor blade. Though not shown here, some results for initial response to collective input were derived using a somewhat more accurate representation of the reverse-flow region.[6] Though the exact values for rotor torque were slightly different between the two methods at high advance ratio, the results regarding the sign of the rotor torque were completely consistent with those shown in Fig. 2.

Secondary responses of the aircraft include an altitude gain directly resulting from the increased rotor thrust (brought on by increased rotor thrust) and a pitch up as a result of the change in direction of the thrust vector (because of the increase in a_{1_s}, shown in Fig. 3 for the 75-m/s trim point. As the aircraft gains altitude and loses airspeed, Ω decreases again as the rotor inflow is reduced. The

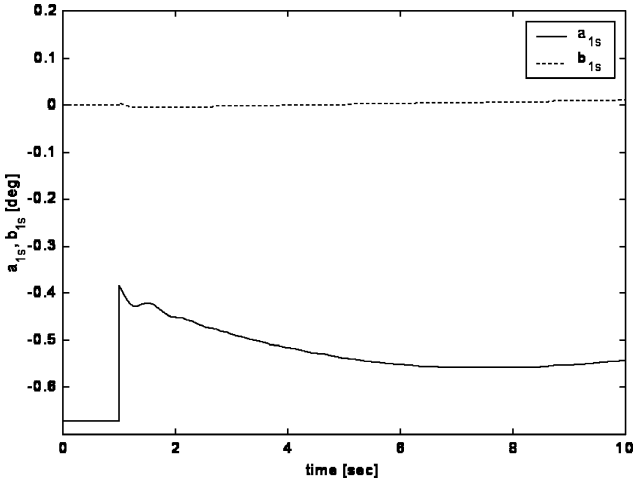

Fig. 3 Rotor flapping response to $\delta\theta_0 = 0.25$ deg.

lateral flapping angle b_{1s} slightly decreases due to the increase in Ω (and tip-speed ratio μ) and then slightly increases as Ω decreases again. The aircraft rolls to the left due to the decrease in lateral flapping angle b_{1s} and then rolls to the right as b_{1s} increases.

Though not included here, the model response to lateral and longitudinal cyclic controls was also tested. Results from these tests may be found in Ref. 7. From observation and analysis of the predicted vehicle response to control inputs, it appears that the ALSR AV AG model performs within an acceptable level of validity for this application and in accordance with dynamics of AG aircraft.

IV. Dynamic Modes and Stability

A. Aircraft Trim

Trim points for the ALSR AV are found using a trim code with a multivariable simplex method minimization algorithm at its core.

Table 2 ALSR AV AG configuration eigenvalues

Mode	Eigenvalues	Damping (ζ)	ω_n [rad/s]
1 (Phugoid AG)	$\lambda_{11,12} = 0.0180 \pm 0.3143i$	-0.0573	0.315
2 (Short-period AG)	$\lambda_{5,6} = -1.7182 \pm 6.8309i$	0.244	7.04
3 (Spiral AG)	$\lambda_{13} = 0.0049$	-1	0.0049
4 (Rolling convergence AG	$\lambda_9 = -4.4661$	1	4.4661
5 (Dutch roll AG)	$\lambda_{7,8} = -0.8467 \pm 7.5284i$	0.112	7.58
6 (Slow convergence)	$\lambda_{10} = -0.5541$	1	0.5541

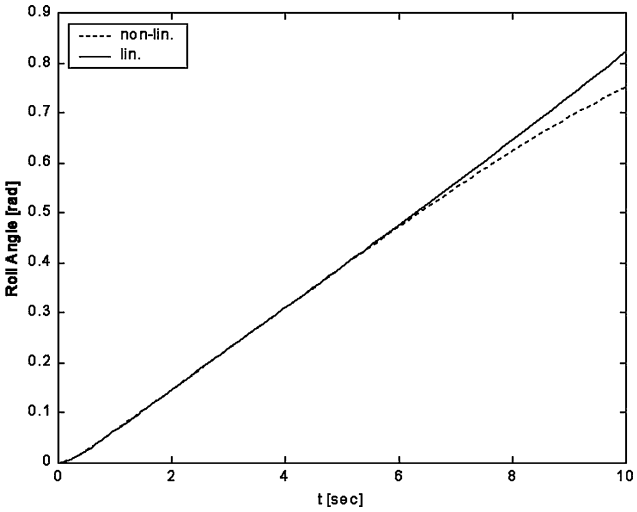

Fig. 4 Roll angle for lateral cyclic step input: $\delta A_1 = 0.25$ deg.

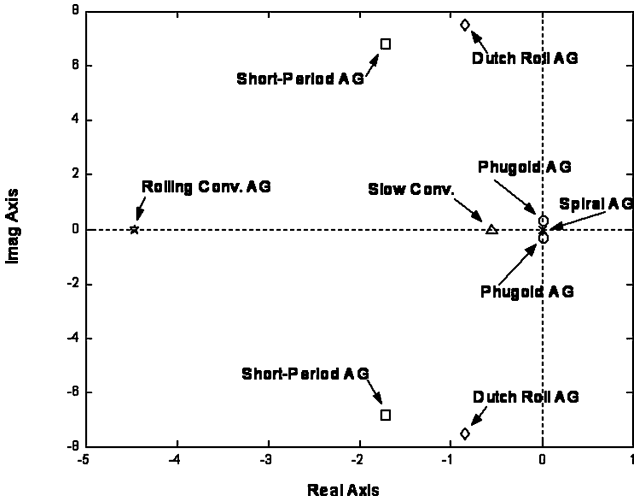

Fig. 5 ALSR AV AG dynamic modes.

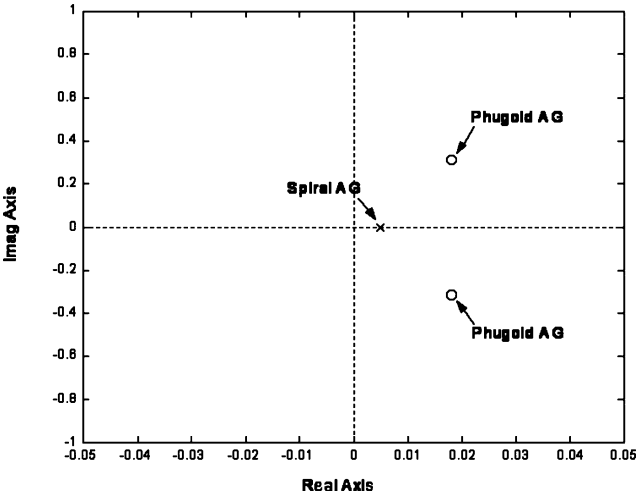

Fig. 6 ALSR AV AG dynamic modes (zoomed in near the origin).

The trim of the aircraft is determined at three equilibrium points. These points correspond to flight conditions chosen for a meaningful analysis. The first point is near the aircraft stall airspeed, the second point is in between the stall airspeed and the maximum airspeed, and the third point is near the maximum airspeed. The three trim points are given in Table 1. The rotor angular velocity of 100 rad/s corresponds to a preselected nominal value.

B. System Linearization

The MATLAB®/Simulink ALSR AV AG nonlinear dynamic model is linearized at each trim point using the MATLAB builtin linearization function linmod, which returns the linear model in conventional state-space form A, B, C, D,

$$\dot{\boldsymbol{x}} = A\boldsymbol{x} + B\boldsymbol{u}, \qquad \boldsymbol{y} = C\boldsymbol{x} + D\boldsymbol{u}$$

with $\boldsymbol{x} = [u, v, w, p, q, r, x_e, y_e, z_e, \phi, \theta, \psi, \Omega]$, $\boldsymbol{u} = [\delta_r, \delta_{e\_L}, \delta_{e\_R}, T_{\text{prop}}, \theta_o, A_1, B_1]$, and $\boldsymbol{y} = [V_\infty, \alpha, \beta, p, q, r, \psi, \theta, \phi, x_e, y_e, -z_e, \Omega]$. The linearized system's state-space matrices A and B for the AG model at an airspeed V_∞ of 53 m/s (trim point 2) are given in the Appendix.

The responses of the ALSR AV linear and nonlinear systems to step commands of the control inputs are compared. The magnitudes of the step control inputs used are large enough to test the limits of the linear systems. Figure 4 shows the responses of the ALSR AV AG flight linear and nonlinear systems to lateral cyclic A_1 step control input. Little difference exists between the linear and nonlinear responses, as expected from an aircraft whose rotational rates are small. Nonlinear effects occur only when angles become large enough that small-angle approximations no longer hold. Comparisons between linear and nonlinear responses were carried out for collective and longitudinal cyclic step inputs with similar results.

C. Small-Disturbance Stability Analysis

The dynamic modes of the ALSR AV in AG configuration are obtained from the state-space system matrix A [Appendix Eqs. (A1) and (A2)], which belongs to the AG model linearized at trim point 2($V_\infty = 53$ m/s, $\gamma = 0$ deg, $\Omega = 100$ rad/s, given in Table 1). The condition of the AG aircraft at $t = 0$ is that of trim point 2, which represents the values of the state variables and control inputs at which the linear model was obtained ($\boldsymbol{x}^*$ and $\boldsymbol{u}^*$). Also, the effect of the airspeed V_∞ on the AG configuration dynamic modes is observed. The dynamic modes of the vehicle in AG configuration are more similar to those of a fixed-wing aircraft than those of a helicopter. This result has also been shown by Houston.[3,4]

Table 2 shows the ALSR AV AG system dynamic modes eigenvalues, damping, and natural frequency. A pole-zero map of the AG dynamic modes is shown in Figs. 5 and 6. The phugoid AG mode is a long-period, slowly divergent oscillation. This mode is dynamically unstable, but its slow divergence makes it easily controllable. The spiral AG mode also has a slow divergence. This mode has extremely long time to double (140 s); therefore, it is easily controllable. The slow convergence mode is a slow convergence (compared to the rolling convergence AG mode). This mode appears due to the extra rotorspeed DOF of the autorotation model, and therefore, it is

Table 3 AG modes: important parameters

Mode	Period T, s	t_{half}, s	N_{half}, cycles
Phugoid AG	19.989	38.401 t_{double}	1.916
Short-period AG	0.920	0.403	0.437
Spiral AG	——	140.194 t_{double}	——
Rolling convergence AG	——	0.155	——
Dutch roll AG	0.835	0.819	0.978
Slow convergence	——	1.251	——

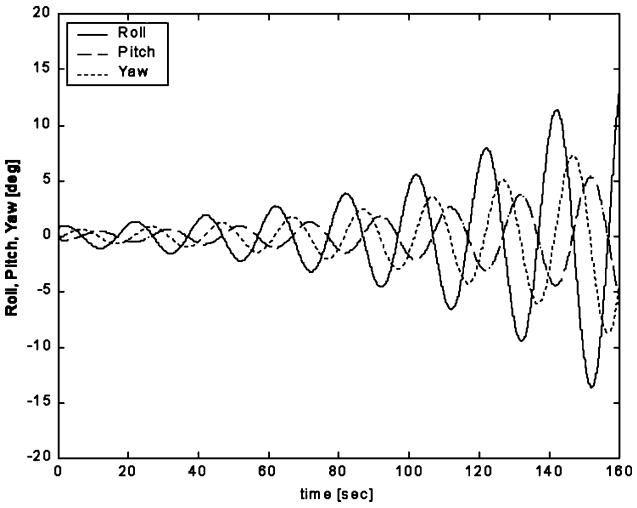

Fig. 7 Phugoid AG mode: aircraft attitude vs time.

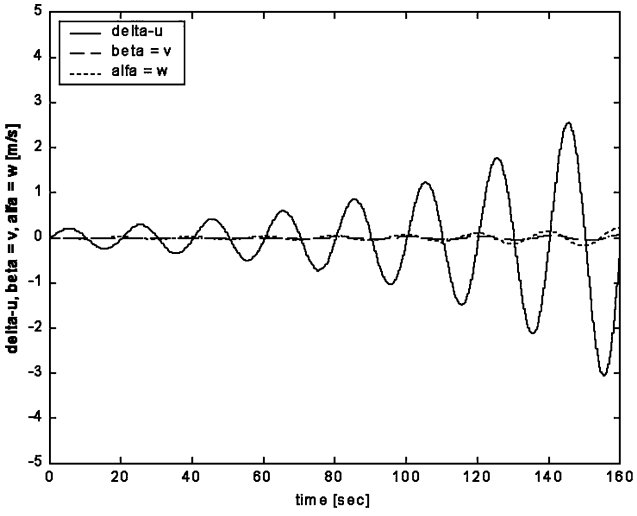

Fig. 8 Phugoid AG mode: aircraft velocities vs time.

also named the rotorspeed mode by Houston.[3] All other modes are stable and similar to those of a standard fixed-wing aircraft.

The longitudinal and lateral motions of the ALSR AV in the AG configuration do not become decoupled. The reason for this is the operation of the rotor/wing as a rotor. When the longitudinal variables vary, they produce a change in the rotor/wing angular velocity, which in turn produces a change in the lateral flapping angle, which then causes the aircraft to roll and then yaw. All of the AG dynamic modes have longitudinal–lateral coupling to some degree. The coupling that results from the inclusion of the rotorspeed DOF is also noted by Houston.[3,8] Table 3 shows the period T, time to half or double t_{half}, and cycles to half or double N_{half} of the AG modes.

The most interesting of these modes is the phugoid, the behavior of which is shown in Figs. 7–11. The attitude behavior is one of

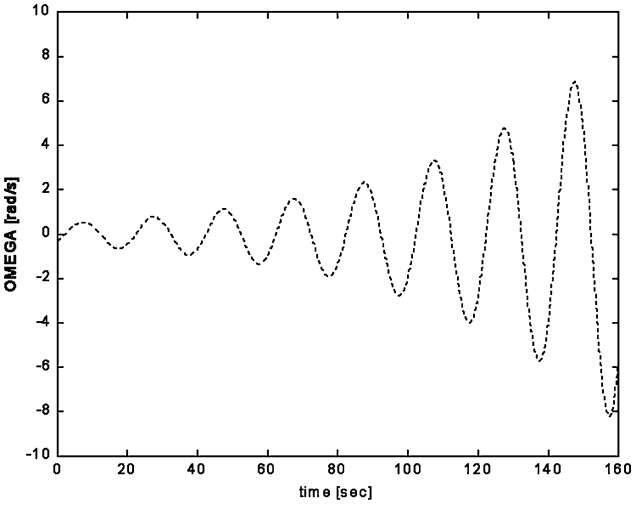

Fig. 9 Phugoid AG mode: $\Delta\Omega$ vs time.

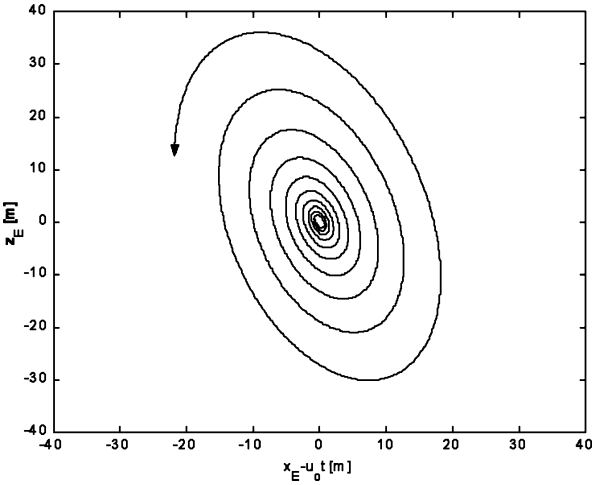

Fig. 10 Phugoid mode: flightpath (xz plane, $u_o t$ moving frame).

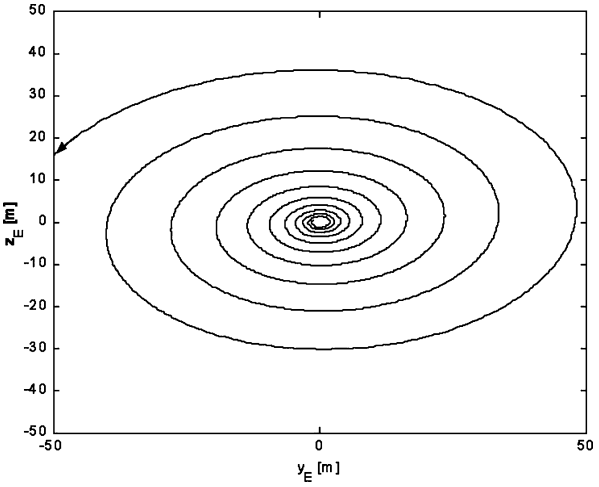

Fig. 11 Phugoid mode: flightpath (yz plane, front view).

variation in pitch θ, roll ϕ, and yaw ψ. The roll is opposite to the pitch oscillation by a phase angle of about 180 deg, whereas the roll oscillation leads the yaw by a phase angle of about 90 deg. The velocity behavior is one of large variation in u and a small variation in w (α), whereas variation in v (β) is very small. The oscillation in w leads the oscillation of u by a phase angle of about 90 deg. The variation of the rotor/wing angular velocity Ω is relatively large, and its oscillation is lagging oscillation in aircraft airspeed u by a

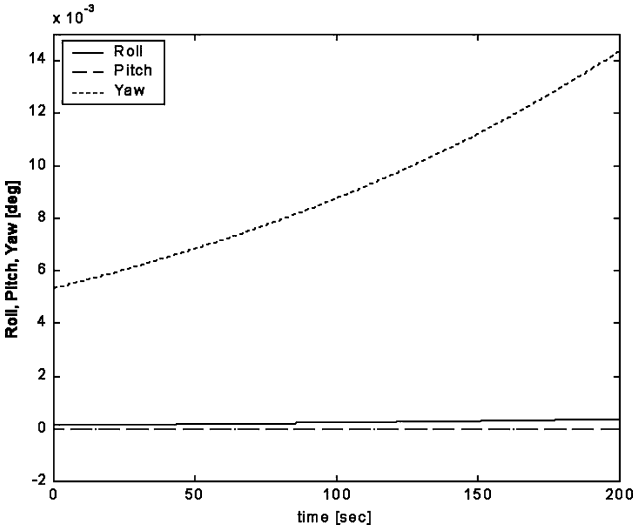

Fig. 12 Spiral AG mode: aircraft attitude vs time.

small phase angle. Additional insight can be gained looking at the path described by the ALSR AV in the xz plane relative to axes moving at the reference speed u_o. It can be deduced that as the AG ALSR AV is close to the bottom of the wave, its forward airspeed is the highest, whereas close to the top of the wave, its airspeed is the lowest (Fig. 10). The motion shows an exchange between potential energy and kinetic energy, including the rotational kinetic energy of the rotor. Figure 11 shows the path that the AG aircraft describes in the yz plane as the observer captures a front view. It can be deduced that the lateral velocity with respect to the Earth, $\dot{y}_e$ is the highest as the aircraft reaches the bottom of the wave; $-\dot{y}_e$ is the highest as the aircraft reaches the top of the wave. Because the angular velocity of the rotor/wing, Ω; is near the highest at the bottom of the wave (when u is at the highest), the lateral flapping angle b_{1s} is also near its highest at the bottom of the wave, and therefore, $\dot{y}_e$ is at its highest at that point (as shown in Fig. 11). This is of the same nature as the conventional-flight phugoid mode motion, the main difference being that the AG phugoid energy exchange includes the rotation of the rotor and a small sideways component of velocity. Houston has shown that the phugoid mode will tend to be destabilized by coupling with the rotorspeed DOF.[8] A possible solution to this instability could be to move the rotor/wing shaft farther aft of the aircraft c.g. and to move the propeller thrust line farther below the c.g., this to decrease the aircraft derivatives Q_u, M_Ω, and M_w (Refs. 3 and 8). The mode takes about 38 s for its motion to double, making it easily controllable.

Figure 12 shows the behavior of the spiral AG mode. The attitude behavior consists of a relatively large divergence of yaw ψ and a small divergence of roll ϕ. The velocity behavior is one of divergence in v ($\approx \beta$) and a very small divergence in u, which may be assumed negligible. The spiral AG mode can be considered the same as the conventional flight spiral mode, only with a larger time to double (about twice) for the case of the ALSR AV, which makes it even more easily controllable.

The rolling-mode takes about 0.15 s to half, and it is highly stable. The attitude behavior is one of rapid subsidence of roll ϕ, in a smaller scale yaw ψ, and in a very small scale pitch θ (which may be considered negligible).

Figures 13 and 14 show the behavior of the Dutch roll AG mode. The attitude behavior is one of large variation in yaw ψ, a small variation in roll ϕ, and a very small variation in pitch θ (which may be considered negligible). The roll oscillation leads the yaw slightly (as the AG ALSR AV reaches maximum roll to the right, it is about to reach maximum yaw to the right). The velocity behavior is one of mainly variation in v (β), whereas variations in w and u are very small and can be assumed negligible. The phase angle between the sideslip ($\beta \approx v$) and the yaw is of about 180 deg, which means that as the aircraft reaches maximum yaw to the right the sideslip angle

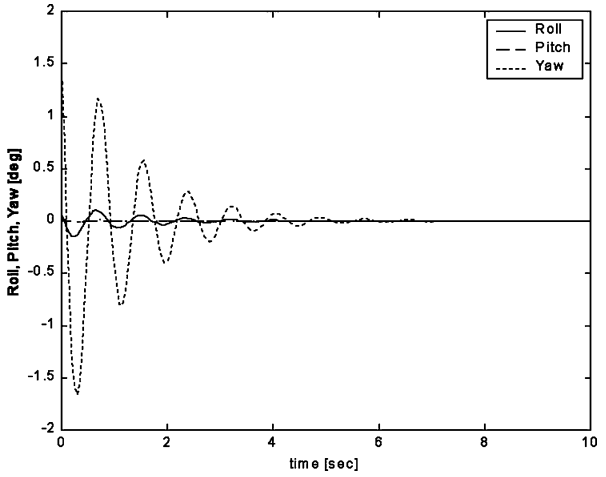

Fig. 13 Dutch roll AG mode: aircraft attitude vs time.

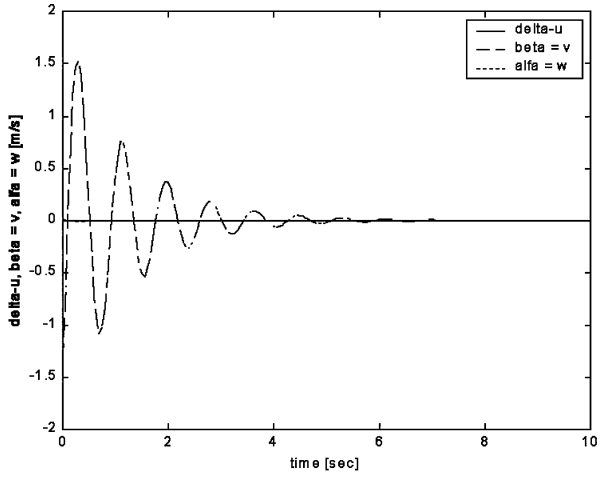

Fig. 14 Dutch roll AG mode: aircraft velocities vs time.

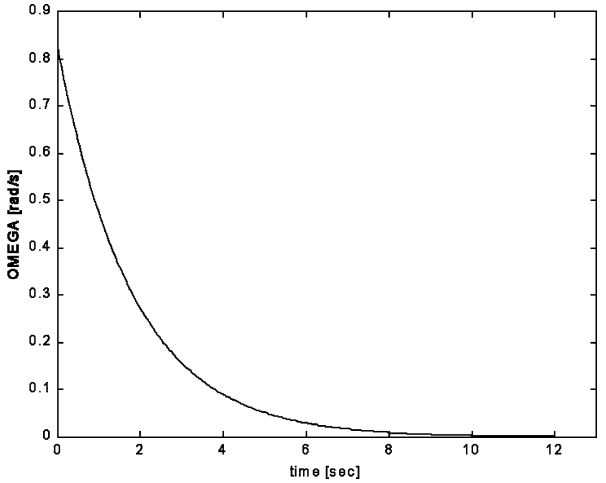

Fig. 15 Slow convergence AG mode: $\Delta\Omega$ vs time.

is at its maximum negative value. The variation of the rotor/wing angular velocity Ω is relatively small. The mode time to half is of 0.819 s, approximately double of the short-period AG time to half of 0.403 s.

Figure 15 shows the behavior of the slow convergence AG mode. This mode is normally not associated with conventional aircraft dynamics and is introduced because of the additional rotor DOF. The behavior is one of relatively large subsidence of the rotor/wing

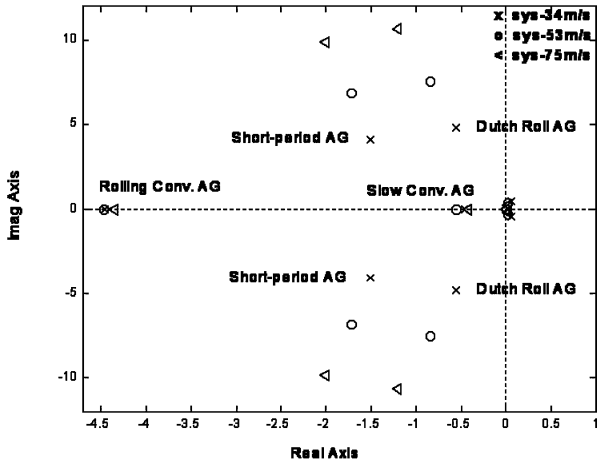

Fig. 16 AG configuration eigenvalues vs airspeed.

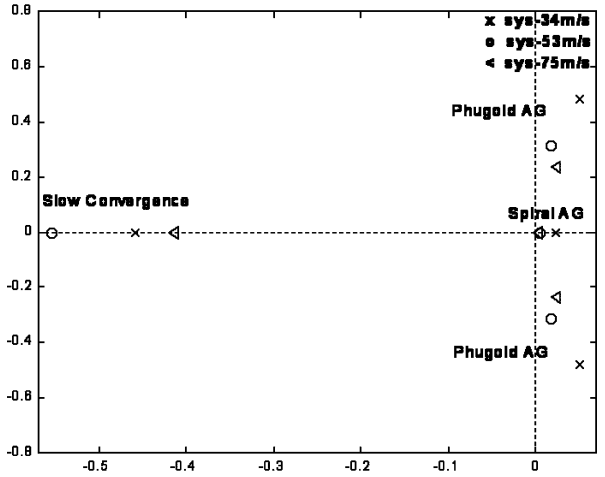

Fig. 17 AG configuration eigenvalues vs airspeed (zoomed in near the origin).

angular velocity Ω (rotorspeed damping). The mode takes about 1.51 s to half.

Figures 16 and 17 show the location of the ALSR AV AG configuration dynamic mode poles at different level-flight airspeeds. The airspeeds are taken from the AG trim points given in Table 1; these are 34, 53, and 75 m/s. The dynamic modes are extracted from linearized systems at each trim point. It can be observed that the short-period AG mode increases its oscillation frequency and becomes more damped as the airspeed increases. (It becomes more stable.) Similarly, the Dutch roll AG mode increases its oscillation frequency and becomes more damped. The rolling convergence AG mode pole moves a little to the left and then a little to the right on the real axis to end slightly less damped at 75 m/s than originally (at 34 m/s). The slow convergence (rotorspeed) mode pole moves similarly to the rolling convergence AG pole, that is, a little to the left and then to right to end slightly less damped. The spiral AG mode becomes less unstable as the airspeed increases (Fig. 17). (Pole moves closer to the imaginary axes.) Finally, the phugoid AG mode decreases in oscillatory frequency, as its poles move closer to the real axis at 53 m/s, to recede a little again at 75 m/s (remaining more stable than at 34 m/s).

The ALSR AV in AG flight mode is slightly unstable due to its phugoid AG mode ($t_{\text{double}} = 38.4$ s) and its spiral AG mode ($t_{\text{double}} = 140.1$ s). Both instabilities can effectively be controlled by an automatic stability augmentation system. The overall stability of the AG ALSR AV increases as its airspeed increases (with in the AG flight envelope).

V. Control Response

This section details the influence of the dynamic modes in the response to the selected controls and the control effectiveness of the rotor controls and the elevons. In conventional flight, rudder input δ_r controls yaw, elevon input δ_{elevon} controls roll, and elevator input δ_{elevator} controls pitch. For AG flight, however, lateral cyclic A_1 is selected to control roll, longitudinal cyclic B_1 is initially selected to control pitch, and rudder δ_r is selected to control yaw. A control sequence for mid-flight mode conversion, which combines all of the controls in an optimal way is the aim of future work.

Because the effective range of flap actuation (rudder or elevons) is about ± 60 deg and the effective range of rotor/wing control actuation (collective pitch or cyclic) is about ± 10 deg, it is assumed that 1 deg of conventional control (δ_{rudder}, δ_{elevons}, and $\delta_{\text{elevators}}$) is equivalent to 0.166 deg of rotor/wing control ($\delta\theta_o$, δA_1, and δB_1).

Figures 18 and 19 show the roll-rate p and roll-angle ϕ response of the AG ALSR AV to a lateral cyclic step input ΔA_1-0.166 deg. The roll-rate response is mainly dominated by the rolling convergence AG mode, but there is also a small presence of the phugoid AG mode (illustrating the longitudinal–lateral motion coupling in AG flight). The roll-angle response is almost linear with a superimposed small variation due to the persistent small phugoid oscillation in the roll rate and a small presence of the spiral AG mode divergence. The non-dominating modes are difficult to discern in Figs. 18 and 19, though small perturbations representing the influence of the phugoid AG are noticeable in Fig. 19. The effect of the spiral AG does not become apparent until much larger time than is shown in Figs. 18 and 19.

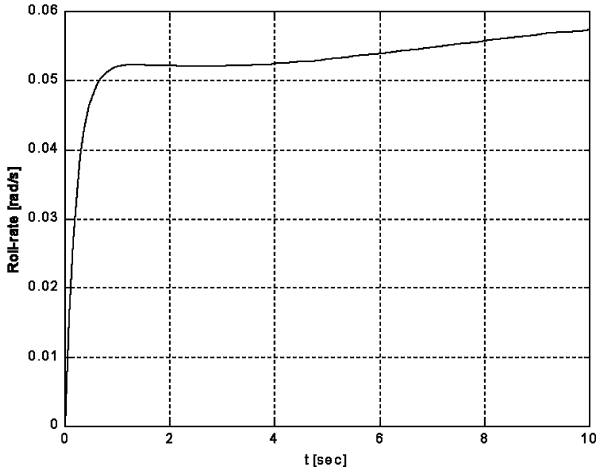

Fig. 18 Roll-rate p response to $\Delta A_1 = 0.166$ deg.

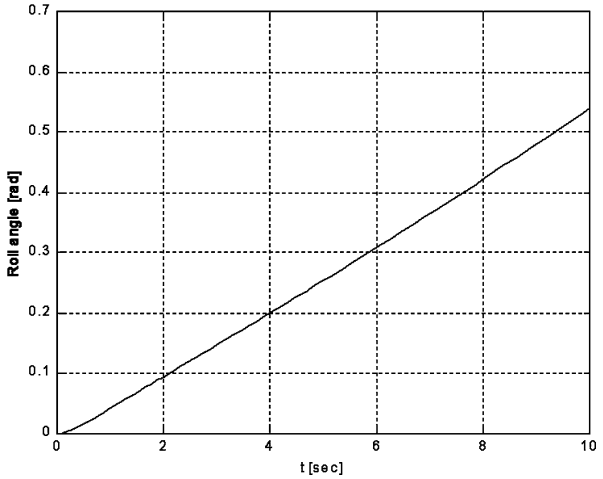

Fig. 19 Roll ϕ response to $\Delta A_1 = 0.166$ deg.

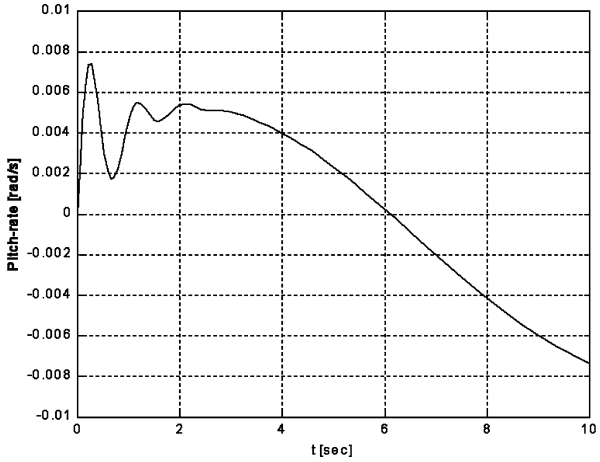

Fig. 20 Pitch-rate q response to $\Delta B_1 = -0.166$ deg.

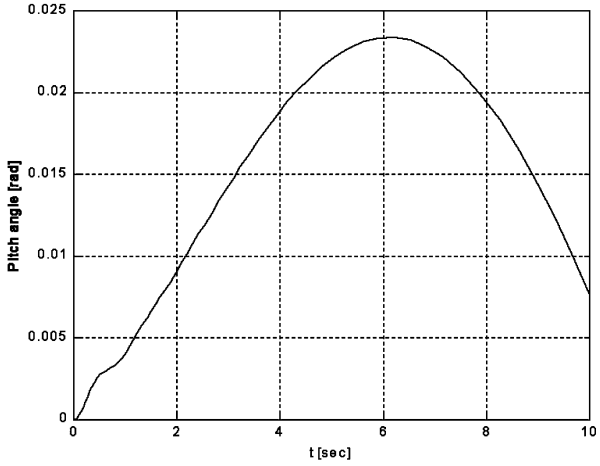

Fig. 21 Pitch θ response to $\Delta B_1 = -0.166$ deg.

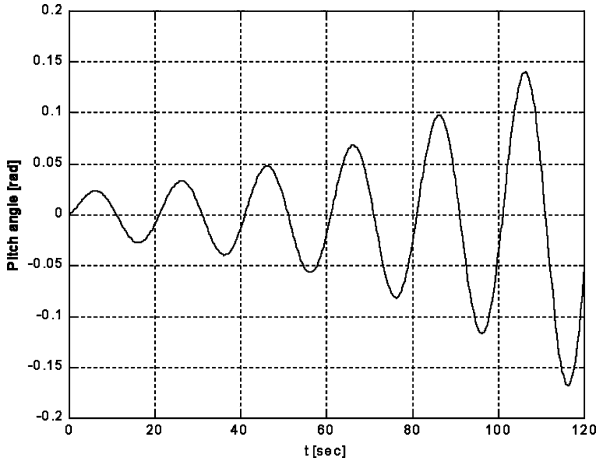

Fig. 22 Pitch θ response to $\Delta B_1 = -0.166$ deg.

Figures 20 and 21 show the pitch-rate q and pitch-angle θ response of the AG aircraft to a longitudinal cyclic step input ΔB_1 -0.166 deg. The pitch-rate variation is composed of the high-frequency heavily damped short-period AG mode oscillation and the low-frequency phugoid AG mode oscillation. The pitch-angle response shows an initial influence of the short-period AG mode and a following dominance of the phugoid AG mode. Figure 22 shows the dynamically unstable long-time response in pitch, where the dominance of the phugoid AG mode can be seen.

Figures 23 and 24 show the yaw-rate r and yaw-angle response ψ of the AG flight ALSR AV to a rudder step input of 1 deg. The yaw-rate response is composed of the Dutch roll AG mode and a linear variation, the latter due to the yawing force generated by the rudder. The heavily damped Dutch roll AG mode disappears quickly as the linear variation remains. The long-time yaw-angle response is also influenced by the spiral AG mode divergence.

Table 4 Roll control effectiveness in conventional and AG configuration

V_∞, m/s	Sensitivity, rad/s^2 · deg	Roll acceleration $\Delta_{\dot{p}}$ equivalent control actuation, rad/s^2
	Conventional $\Delta\delta_{\text{elevon}} = 1$ *deg*	
60	$\left[\frac{\partial \dot{p}}{\partial \delta_{\text{elevon}}}\right] = 0.2252$	0.2252
75	$\left[\frac{\partial \dot{p}}{\partial \delta_{\text{elevon}}}\right] = 0.3436$	0.3436
86	$\left[\frac{\partial \dot{p}}{\partial \delta_{\text{elevon}}}\right] = 0.4504$	0.4504
	AG $\Delta A_1 = 0.166$ *deg*	
34	$\left[\frac{\partial \dot{p}}{\partial A_1}\right] = 1.4155$	0.2350
53	$\left[\frac{\partial \dot{p}}{\partial A_1}\right] = 1.4373$	0.2386
75	$\left[\frac{\partial \dot{p}}{\partial A_1}\right] = 1.4556$	0.2416

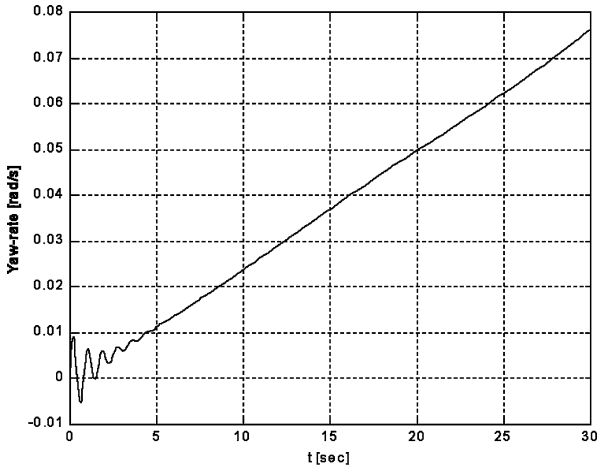

Fig. 23 Yaw-rate r response to rudder ($\Delta\delta_r = 1$ deg).

Table 4 shows a study of the ALSR AV roll control effectiveness. The elevons (in conventional and AG flight) and the lateral cyclic control (in AG flight) are chosen to control roll. The right most column of Table 4 gives the roll acceleration produced by equivalent control actuations. The elevon effectiveness increases as the airspeed of the aircraft increases, as expected. The roll acceleration $\Delta\dot{p}$ produced at 86 m/s is of 0.4504 rad/s^2, which is about the double of 0.2252 rad/s^2, produced at 60 m/s. The elevon roll control is still effective at 60 m/s (near conventional flight stall speed). With a functional flap deflection of 60 deg, the elevon control could produce a maximum roll acceleration of 13.512 rad/s^2 as the conventional ALSR AV flies at an airspeed of 60 m/s. In the case of AG flight, the lateral cyclic control effectiveness is almost nondependent on the airspeed. As it can be observed, the roll acceleration produced by ΔA_1 at 34 m/s is 0.2350 rad/s^2 and at 75 m/s is 0.2416 rad/s^2, a very slight increase. Roll control effectiveness of A_1 at 34 m/s is acceptable considering that maximum roll acceleration using $\Delta A_1 = 10$ deg is 14.1 rad/s^2. From the preceding observations, it can be concluded that elevon effectiveness is good through the conventional configuration flight envelope (about 60–86 m/s). It is also concluded that the lateral cyclic control is effective through

Table 5 Pitch control effectiveness in conventional and AG configuration

V_∞, m/s	Sensitivity, rad/s^2 · deg	Pitch acceleration $\Delta_{\dot{p}}$ equivalent control actuation, rad/s^2
	Conventional $\Delta\delta_{\text{elevator}} = 1$ *deg*	
60	$\left[\frac{\partial \dot{q}}{\partial \delta_{\text{elevator}}}\right] = 0.2960$	0.2960
75	$\left[\frac{\partial \dot{q}}{\partial \delta_{\text{elevator}}}\right] = 0.4516$	0.4516
86	$\left[\frac{\partial \dot{q}}{\partial \delta_{\text{elevator}}}\right] = 0.5918$	0.5918
	AG, $\Delta B_1 = -0.166$ *deg*	
34	$\left[\frac{\partial \dot{q}}{\partial B_1}\right] = -0.3511$	0.0583
53	$\left[\frac{\partial \dot{q}}{\partial B_1}\right] = -0.3233$	0.0537
75	$\left[\frac{\partial \dot{q}}{\partial B_1}\right] = -0.2838$	0.0471

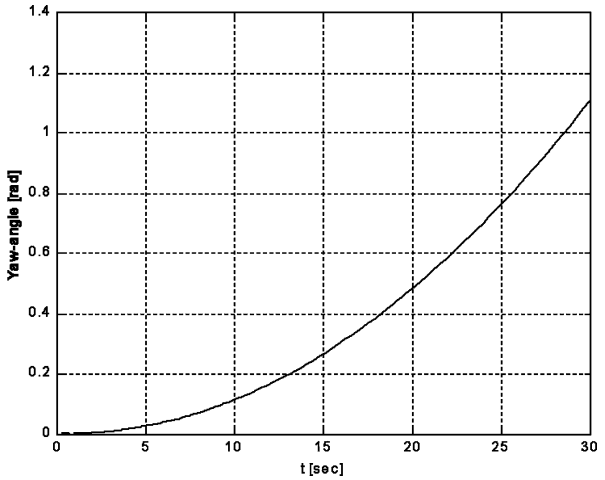

Fig. 24 Yaw ψ response to rudder ($\Delta\delta_r$ = 1 deg).

the AG flight envelope (about 34–75 m/s). Finally, it is concluded that in AG flight where the elevon control is also operational it is advisable to use elevon control above 60 m/s and lateral cyclic control below 60 m/s.

Table 5 shows a study of the ALSR AV pitch control effectiveness. To control pitch, the elevator (in conventional and AG flight) and the longitudinal cyclic control (in AG flight) are chosen. The pitch acceleration $\Delta\dot{q}$ produced at 60 m/s is 0.2960 rad/s^2 and at 86 m/s is 0.5918 rad/s^2; therefore, the elevator pitch effectiveness increases by a about a factor of two from 60 to 86 m/s. The elevator pitch control at 60 m/s is good, with an estimated maximum pitch acceleration of 17.76 rad/s^2 from a 60-deg deflection. In the case of AG flight, longitudinal cyclic control B_1 effectiveness is slightly inversely proportional to airspeed (at 34 m/s $\Delta\dot{q}$ is 0.0583 rad/s^2, whereas at 75 m/s $\Delta\dot{q}$ is 0.0471 rad/s^2). Pitch control effectiveness of B_1 at 34 m/s while at its highest is still low, with an estimated maximum pitch acceleration of 3.5 rad/s^2 from a 10-deg B_1 actuation. In AG flight at 34 m/s, elevator pitch control effectiveness is higher than that of the longitudinal cyclic with a pitch acceleration of 0.0914 rad/s^2 per 1-deg deflection and an estimated maximum of 5.484 rad/s^2 from a 60-deg deflection. (These values are not shown in Table 5). From the preceding observations, it can be concluded that elevator pitch control effectiveness is good through the conventional configuration flight envelope and that the longitudinal cyclic pitch control effectiveness is poor through the AG flight envelope. It is, therefore, also concluded that in AG flight the elevator should be used to supplement the longitudinal cyclic to control pitch.

Table 6 Yaw control effectiveness in conventional and AG configuration, $\Delta\delta_{\text{rudder}}$ = 1 deg

V_∞, m/s	Sensitivity $\frac{\partial r}{\partial \delta_{\text{rudder}}}$ rad/s^2 · deg	Yaw acceleration $\Delta\dot{r}$ equivalent control actuation, rad/s^2
	Conventional	
60	0.1057	0.1057
75	0.1623	0.1623
86	0.2126	0.2126
	AG	
34	0.0334	0.0334
53	0.0807	0.0807
75	0.1616	0.1616

Table 6 shows a study of the ALSR AV yaw control effectiveness. To control yaw in conventional and AG flight configuration, the rudder is chosen. Rudder effectiveness increases as the airspeed of the aircraft increases in both configurations. The yaw acceleration produced by 1 deg of rudder deflection at 34 m/s is 0.0334 rad/s^2, whereas at 86 m/s it is 0.2126 rad/s^2. Rudder yaw control effectiveness at 34 m/s is low with an estimated maximum yaw acceleration of 2.004 rad/s^2 from a 60-deg rudder deflection. At 53 m/s, yaw effectiveness becomes acceptable with a maximum yaw acceleration of 4.842 rad/s^2 from a 60-deg deflection. It can be concluded that, for most of the AG and conventional flight envelope, rudder yaw control effectiveness is good. Also note that rudder effectiveness at airspeeds below 53 m/s may be higher than estimated due to the propeller airstream (if turboprop engine option is chosen instead of turbofan). Further research must be done to analyze the effect of the propeller airstream and rotor/wing wake in rudder yaw control effectiveness. In the case that rudder effectiveness remains low at low speeds, the area of the rudder control surface may be increased.

VI. Conclusions

The paper describes a procedure for modeling the dynamics and aerodynamics of an autorotating rotor/wing UAV aircraft. The model is verified by observing responses to given control inputs and comparing with expected results. The responses of the autorotation flight model conform for the most part to known aircraft/AG dynamics, although the rotor speed response to collective input shows an unexpected result at high advance ratio. This result, that the rotor speed increases in response to a step increase in collective input, occurs only at mid-to-high advance ratio and can be explained by noting the relative importance of each term in the rotor inflow equation as the advance ratio varies. The trend appears to be correct, at least to within the limits of the model.

Stability analysis to small disturbances is performed at each of three equilibrium trim points, and the dynamic modes of the aircraft in autorotation configuration were investigated. Six dynamic modes for the AG aircraft are identified; the modes correspond closely to conventional aircraft dynamic modes with the exception of an additional slow-convergence mode associated with the rotor angular velocity DOF. The ALSR AV is slightly unstable in the phugoid AG mode and the spiral AG mode. Both instabilities should be easily controllable. The overall stability of the AG ALSR AV increases as its airspeed increases.

For roll control, elevon effectiveness is good throughout the conventional configuration flight envelope (about 60–86 m/s, not shown in the results of this paper). It is also concluded that the lateral cyclic control is effective through the AG flight envelope (about 34–75 m/s). Finally, it is concluded that in AG flight, where the elevon control is also operational, it is advisable to use elevon control above 60 m/s and lateral cyclic control below 60 m/s.

Elevator pitch control effectiveness is good throughout the conventional configuration flight regime, but longitudinal cyclic pitch

control effectiveness is poor through the AG flight envelope. It is, therefore, recommended that, in AG flight, the elevator be used in conjunction with longitudinal cyclic to control pitch. Further research must be conducted in the area of low-speed pitch controllability during the recovering process.

For most of the AG and conventional flight envelope, rudder yaw control effectiveness is good. Also note that rudder effectiveness at airspeeds below 53 m/s may be better than estimated because the propeller slipstream effects have not been included in this analysis. Further research must be completed to analyze the effect of the propeller airstream and rotor/wing wake in rudder yaw control effectiveness. In the case that rudder effectiveness remains low at low speeds, the area of the rudder control surface may be increased.

Appendix: Linearized System Matrices

The linearized model for the ALSR AV in AG mode flying at trim point 2 ($V_\infty = 53$ m/s, $\gamma = 0$ deg, $\Omega = 100$ rad/s is given. For space convenience the state-space system matrix $A_{(13\times 13)}$ is divided in two submatrices $A_{1(13\times 6)}$ and $A_{2(13\times 7)}$ as follows:

$$A = [A_1 \mid A_2]$$

$$A_1 = \begin{array}{c|cccccc} & u & v & w & p & q & r \\ \dot{u} & -0.0696 & 0 & -0.1545 & -0.1639 & -0.394 & 0 \\ \dot{v} & -0.0041 & -0.213 & 0.0051 & 0.7919 & -0.0946 & -52.7008 \\ \dot{w} & -0.1046 & 0 & -0.9343 & -0.3759 & 54.7584 & 0 \\ \dot{p} & -0.0338 & 0.0758 & 0.0422 & -4.5022 & -0.7765 & -0.0959 \\ \dot{q} & 0.0776 & 0 & -0.8619 & 0.1577 & -2.7454 & 0 \\ \dot{r} & 0.0012 & 1.0837 & -0.0015 & 0.1537 & 0.0274 & -1.4769 \\ \dot{x}_e & 0.9997 & 0 & 0.025 & 0 & 0 & 0 \\ \dot{y}_e & 0 & 1 & 0 & 0 & 0 & 0 \\ \dot{z}_e & -0.025 & 0 & 0.9997 & 0 & 0 & 0 \\ \dot{\phi} & 0 & 0 & 0 & 1 & 0 & 0.025 \\ \dot{\theta} & 0 & 0 & 0 & 0 & 1 & 0 \\ \dot{\psi} & 0 & 0 & 0 & 0 & 0 & 1.0003 \\ \dot{\Omega} & 1.093 & 0 & 4.6526 & 2.3202 & -13.0288 & 0 \end{array} \tag{A1}$$

$$A_2 = \begin{array}{c|ccccccc} & x_e & y_e & z_e & \phi & \theta & \psi & \Omega \\ \dot{u} & 0 & 0 & 0 & 0 & -9.8069 & 0 & -0.0216 \\ \dot{v} & 0 & 0 & 0 & 9.8069 & 0 & 0 & -0.0037 \\ \dot{w} & 0 & 0 & 0 & 0 & -0.2449 & 0 & -0.2074 \\ \dot{p} & 0 & 0 & 0 & 0 & 0 & 0 & -0.0304 \\ \dot{q} & 0 & 0 & 0 & 0 & 0 & 0 & -0.0275 \\ \dot{r} & 0 & 0 & 0 & 0 & 0 & 0 & 0.0011 \\ \dot{x}_e & 0 & 0 & 0 & 0 & -0.0003 & -0.0003 & 0 \\ \dot{y}_e & 0 & 0 & 0 & -1.3233 & 0 & 53.0165 & 0 \\ \dot{z}_e & 0 & 0 & 0 & 0 & -53.0165 & 0 & 0 \\ \dot{\phi} & 0 & 0 & 0 & 0 & 0 & 0 & 0 \\ \dot{\theta} & 0 & 0 & 0 & 0 & 0 & 0 & 0 \\ \dot{\psi} & 0 & 0 & 0 & 0 & 0 & 0 & 0 \\ \dot{\Omega} & 0 & 0 & 0 & 0 & 0 & 0 & -0.1675 \end{array} \tag{A2}$$

$$B = \begin{array}{c|ccccccc} & \delta_r & \delta_{e\_L} & \delta_{e\_R} & T_{\text{prop}} & \theta_o & A_1 & B_1 \\ \dot{u} & 0 & 0.0005 & 0.0005 & 0.0035 & -0.3849 & 0 & 0.3244 \\ \dot{v} & -0.0169 & 0 & 0 & 0 & 0.0035 & 0.1752 & -0.005 \\ \dot{w} & 0 & -0.0208 & -0.0208 & 0 & -1.6818 & 0 & 0.7078 \\ \dot{p} & 0.0623 & 0.0857 & -0.0857 & 0 & 0.0283 & 1.4373 & -0.0407 \\ \dot{q} & 0 & -0.1127 & -0.1127 & 0 & 0.1263 & 0 & -0.3233 \\ \dot{r} & 0.0807 & 0.0004 & -0.0004 & 0 & -0.0010 & -0.0507 & 0.0014 \\ \dot{x}_e & 0 & 0 & 0 & 0 & 0 & 0 & 0 \\ \dot{y}_e & 0 & 0 & 0 & 0 & 0 & 0 & 0 \\ \dot{z}_e & 0 & 0 & 0 & 0 & 0 & 0 & 0 \\ \dot{\phi} & 0 & 0 & 0 & 0 & 0 & 0 & 0 \\ \dot{\theta} & 0 & 0 & 0 & 0 & 0 & 0 & 0 \\ \dot{\phi} & 0 & 0 & 0 & 0 & 0 & 0 & 0 \\ \dot{\Omega} & 0 & 0 & 0 & 0 & 3.8425 & 0 & -4.3809 \end{array} \tag{A3}$$

References

[1]Rutherford, J. W., "Apparatus for Operating a Wing in Three Modes and System of Use," United States Patent, 6, 244, 537 B1, June 2001.

[2]Rutherford, J. W., and Wells, V. L., "An Air-Launched Self-Recovering Autonomous Vehicle Concept," *Aircraft Design Journal*, Vol. 2, No. 2, 1999, pp. 81–94.

[3]Houston, S. S., "Identification of Autogyro Longitudinal Stability and Control Characteristics," *Journal of Guidance, Control, and Dynamics*, Vol. 21, No. 3, 1998, pp. 391–399.

[4]Houston, S. S., "Validation of a Rotorcraft Mathematical Model for Autogyro Simulation," *Journal of Aircraft*, Vol. 37, No. 3, 2000, pp. 403–409.

[5]Etkin, B., and Reid, L. D., *Dynamics of Flight Stability and Control*, 3rd ed., Wiley, New York, 1996.

[6]Prouty, R. W., *Helicopter Performance, Stability, and Control*, Krieger, Malabar, FL, 1995.

[7]Lopez, C. A., "Rotor/Wing Aircraft Dynamics, Modeling, Simulation, and Open Loop Control Analysis," M.S. Thesis, Mechanical and Aerospace Engineering Dept., Arizona State Univ., Tempe, AZ, Oct. 2002.

[8]Houston, S. S., "Analysis of Rotorcraft Flight Dynamics in Autorotation," *Journal of Guidance, Control, and Dynamics*, Vol. 25, No. 1, 2002, pp. 33–39.